Supporting Information for: Electronic tunability of the frustrated triangular-lattice cluster magnet $LiZn_{2-x}Mo_3O_8$.

John P. Sheckelton,[a,b,c] **James R. Neilson,**[a,b,‡] **and Tyrel M. McQueen**[*a,b,c]

1 Experimental methods

$LiZn_2Mo_3O_8$ was synthesized as previously reported[1]. Polycrystalline $LiZn_2Mo_3O_8$ and stoichiometric amounts of solid I_2 were added to a quartz tube sealed *in vacuo*, taking care to minimize loss of I_2 vapor from sublimation. A temperature gradient of 300 °C to 290 °C was established over the reaction vessel and held for one week, with the $LiZn_2Mo_3O_8/I_2$ on the hot side. Characterization was initially performed using a Bruker D8 Focus powder X-ray diffractometer using copper Kα ($\lambda = 1.540$ Å) radiation and a LynxEye detector. Elemental Si was used (a = 5.43102 Å) as an internal standard for Le Bail[2] refinements. Magnetization and resistivity measurements were performed using a Quantum Design Physical Properties measurement system (PPMS). Temperature-dependent resistivity was measured on polycrystalline pellet pieces using the four-probe method over the range T = 300 K to T = 50 K, at which the samples became too resistive. Samples of higher doping were also too resistive to obtain meaningful numbers. Temperature-dependent magnetic susceptibility was measured on powder samples over the range T = 300 K to T = 2 K. Magnetization as a function of applied field was measured at T = 1.8 K up to a field of $\mu_o H$ = 9 T. Molar magnetic susceptibility, defined as $\chi_m = \partial M/\partial H$ as $H \longrightarrow 0$ is approximated here as the DC magnetization over field, M/H. Inverse susceptibility was corrected for a temperature-independent contribution, χ_o, by assuming paramagnetic behavior in the high temperature ($T \geq$150 K) regime and adjusting the value of χ_o until the inverse susceptibility became linear.

High-resolution synchrotron X-ray diffraction (SXRD) experiments were carried out on powder samples of native $LiZn_2Mo_3O_8$ and $2x \leq 0.40$ doped $LiZn_{2-x}Mo_3O_8$ samples using beamline 11-BM-B for Rietveld analysis and beamline 11-ID-B for Pair-distribution function (PDF) analysis at Argonne National Laboratory (APS)[3]. Measurements were taken on powder-coated, greased kapton capillaries at T = 300, 150, and 6 K using a photon wavelength of $\lambda = 0.4139(1)$ Å (≈30 KeV) over the range $0 \leq 2\theta \leq 45$ with a 0.001° 2θ stepsize and a measurement time of 0.1 s per step. Diffraction scans at T = 6 K were taken using an Oxford Cryosystems helium cryostat. Reitveld refinements[4] to the diffraction data were performed using the Bruker Topas professional software suite and the FullProf suite[5]. Powder neutron diffraction on a sample of undoped $LiZn_2Mo_3O_8$ at T = 300 K with d-spacing of 0.2760 Å $\leq d \leq$ 3.0906 Å and 1.6557 Å $\leq d \leq$ 8.2415 Å was performed at the POWGEN diffractometer at the Spallation Neutron Source at Oak Ridge National Laboratory (ORNL). A combined refinement to X-ray/Neutron data on the same sample of undoped $LiZn_2Mo_3O_8$ was performed to freely refine the lithium and zinc occupancies. Subsequent doped samples, with only SXRD scans, assume, based on the observation of only ZnI_2 from doping, fixed lithium occupancies extracted from the combined X-ray/neutron refinement on $LiZn_2Mo_3O_8$. Total scattering powder diffraction patterns for PDF analysis were collected on beamline 11-ID-B at T = 300 K using a Perkin Elmer amorphous silicon detector in a flat-plate geometry and CeO_2 as a calibration standard. Wavelengths of $\lambda = 0.2128$ Å ($\approx$ 60 KeV) and $\lambda = 0.1370$ Å ($\approx$ 90 KeV) were used. Approximate sample-to-detector distances of 18 and 22 cm were used for each sample changer and precise distances were extracted from refinements to the CeO_2 standard. Samples were sealed in kapton tubes and diffraction patterns were collected by summing 120 scans, at a 1 second beam exposure for each scan. PDF analysis was performed on $G(r)$, extracted with a $Q_{max} = 25$ Å^{-1} using PDFgetX2[6]. Powder neutron diffraction patterns suitable for PDF analysis were performed on undoped Li-7 isotopically enriched $LiZn_2Mo_3O_8$ at the NOMAD diffractometer at ORNL, at temperatures ranging from T = 2 K to T = 300 K. PDF analysis was performed on $G(r)$ extracted from data reduced using in-house scripts. Least-squares refinements to $G(r)$ were performed using PDFgui[7]. Refined structures were visualized with VESTA[8].

---

[a] *Department of Chemistry, The Johns Hopkins University, Baltimore, MD 21218, USA.*
[b] *Institute for Quantum Matter, Department of Physics and Astronomy, The Johns Hopkins University, Baltimore, Maryland 21218, USA.*
[c] *Department of Materials Science and Engineering, The Johns Hopkins University, Baltimore, Maryland 21218, USA.*
[‡] Present Address: Department of Chemistry, Colorado State University, Ft. Collins, Colorado 80523, USA.
[*] E-mail: mcqueen@jhu.edu

Molecular density functional theory (DFT) calculations were performed as previously reported[1] using PBE0 hybrid functionals at the UHF level level of theory on the cluster $Mo_3O_4(OH)_3(H_2O)_6$, isoelectronic to a Mo_3O_{13} cluster in $LiZn_2Mo_3O_8$. The GAMESS[9] software package was used for calculations and MacMolPlot[10] for visualization of orbitals and energies. Band structure calculations were performed on $LiZn_2Mo_3O_8$ and doped $LiZn_2Mo_3O_8$ models accounting for spin orbit coupling and a Hubbard U of 2 eV using the ELK all-electron full-potential linearized augmented-plane wave (FP-LAPW) code (Available under the GNU General Public License at elk.sourceforge.net). To simplify calculations, a $LiZn_2Mo_3O_8$ unit cell in the rhombohedral setting was used. In addition calculations were performed with fully occupied and long-range ordered Li and Zn positions in the unit cell, taking care to have the stoichiometry set to $LiZn_2Mo_3O_8$. The doped $LiZn_2Mo_3O_8$ version is the same exact unit cell, with the Li atoms removed as to achieve a non-magnetic calculation.

2 Laboratory X-ray Diffraction

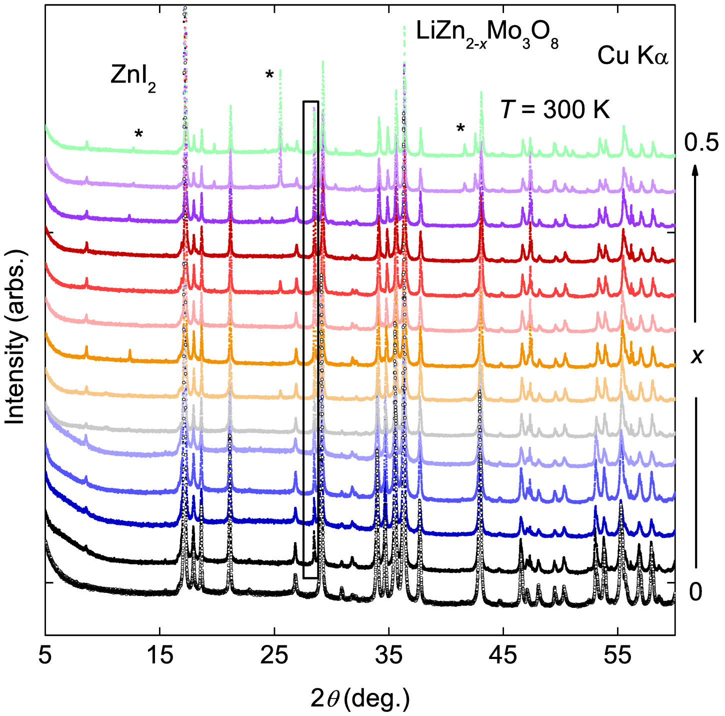

Figure 1 Laboratory powder X-ray diffraction patterns for the entire series of $LiZn_{2-x}Mo_3O_8$. The box highlights the strongest reflection coming from the added silicon standard. The highest doped samples show reflections identified as belonging to ZnI_2 (marked with *), with some samples also showing reflections identified as SiO_2 from breaking of the quartz ampoules.

3 Magnetic Susceptibility

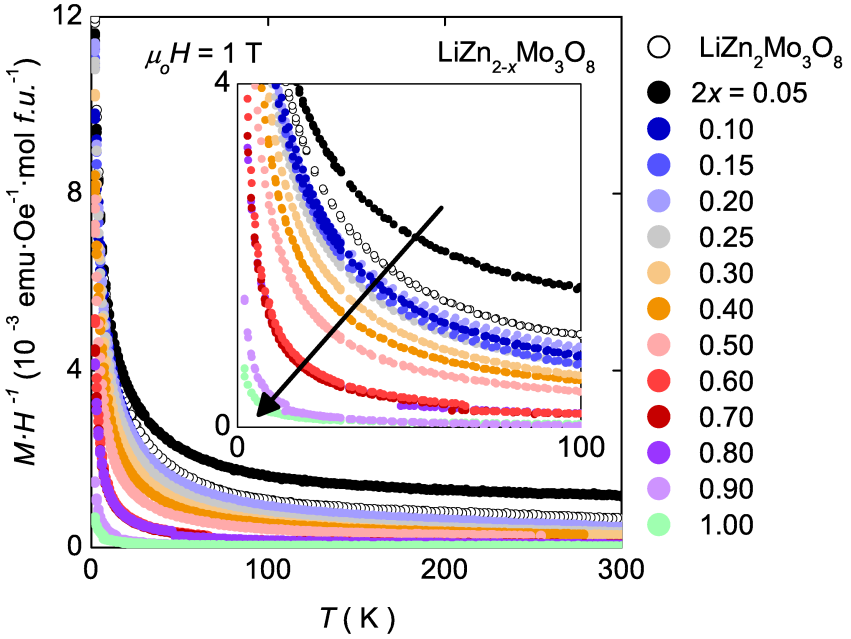

Figure 2 Magnetic susceptibility as a function of temperature for the $LiZn_{2-x}Mo_3O_8$ series. A trend of decreasing susceptibility is observed. The small discontinuities observed in some of the datasets are experimental artifacts from the small measured signal size.

4 Resistivity

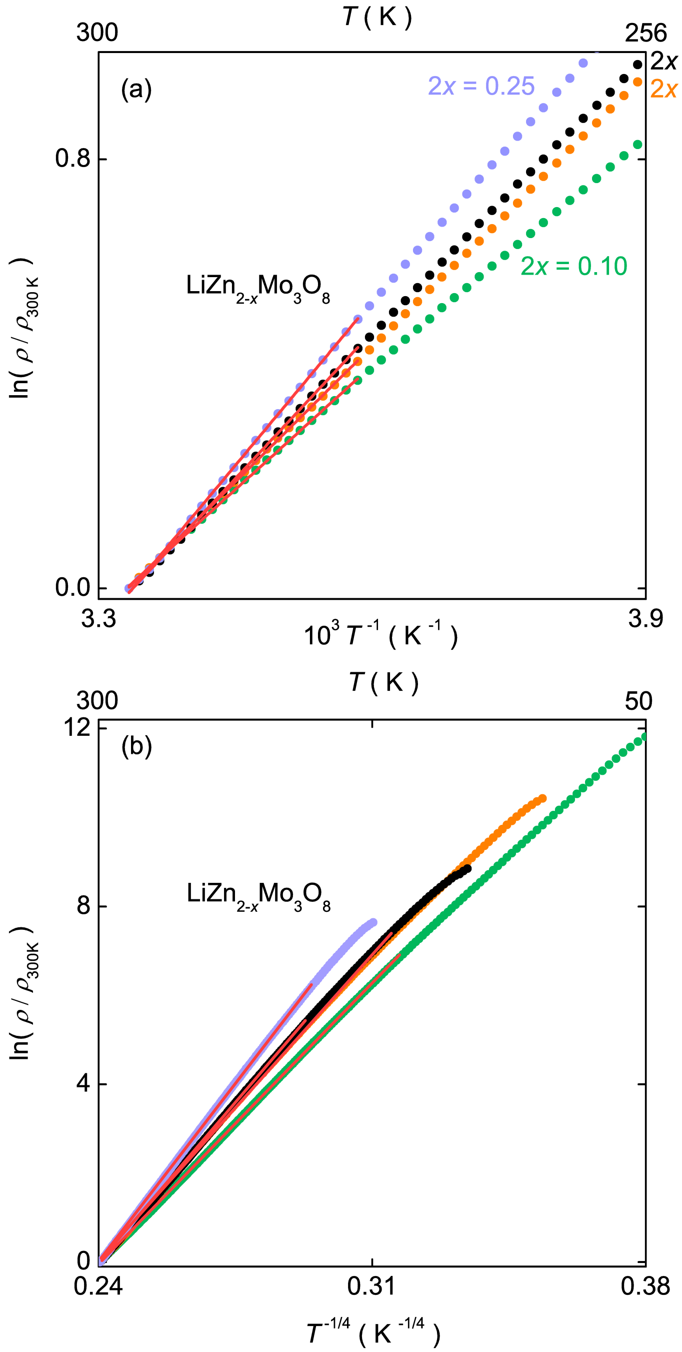

Figure 3 (a) Natural logarithm of normalized resistivity as a function of $\frac{1}{T}$ measured on pellets of $\mathrm{LiZn}_{2-x}\mathrm{Mo}_3\mathrm{O}_8$ samples (b)-(e) with fits to $ln\frac{\rho}{\rho_{300K}} = \frac{E_g}{k_B}\frac{1}{T}$ at high temperature (red lines), used to extract the effective bandgap. (b) The same normalised resistivity in (a), but plotted vs. $\frac{1}{T^{1/4}}$. A $T^{1/4}$ scaling is suggestive of 3-dimensional variable-range-hopping (VRH) and Anderson localization. Plotting $ln\frac{\rho}{\rho_{300K}}$ vs. $\frac{1}{T^{1/4}}$ results in a much larger range of linear behavior, indicating VRH and Anderson localization are occuring in doped samples of $\mathrm{LiZn}_{2-x}\mathrm{Mo}_3\mathrm{O}_8$. Red lines are guides to the eye.

5 Electronic structure

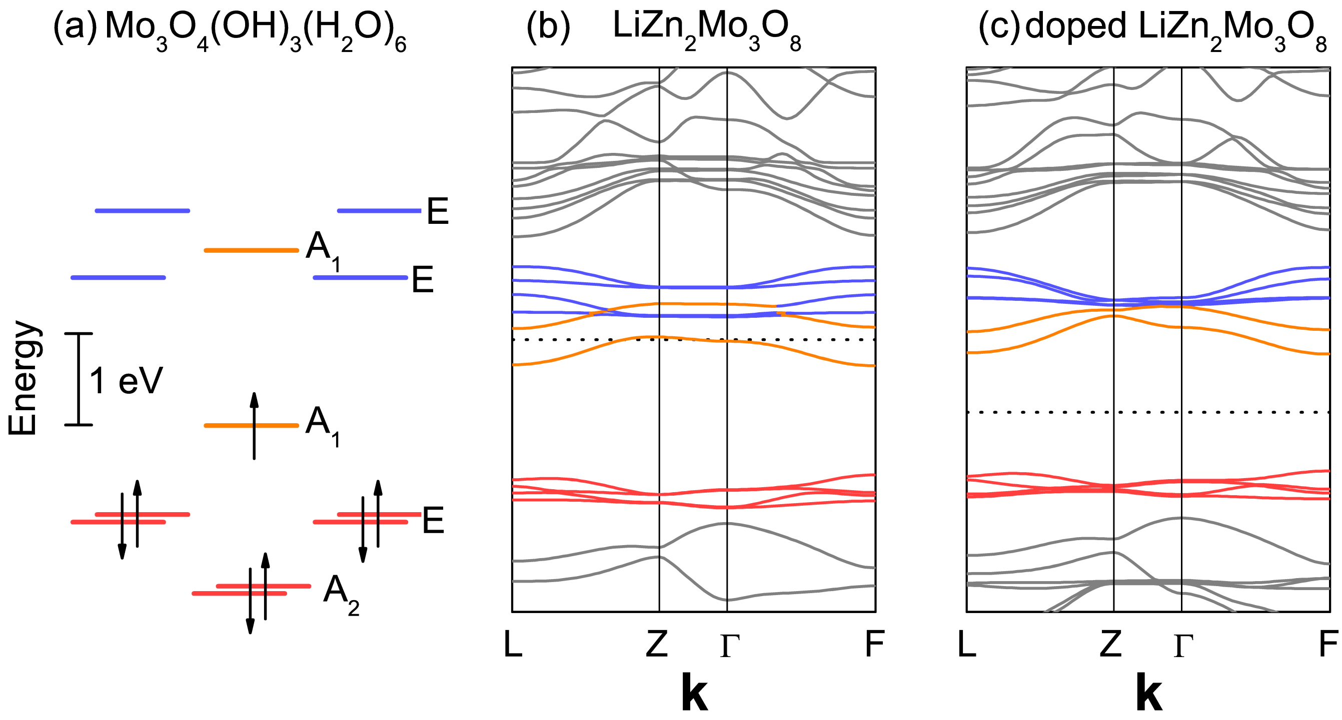

Figure 4 Electronic structure calculations using density functional theory. Plots are offest to lineup the centroid of frontier orbitals. Band structures are calculated in the $R\bar{3}m$ rhombohedral setting, with two Mo_3O_{13} clusters per unit cell. Dashed lines are respective fermi energies. (a) A molecular orbital diagram calculated for $Mo_3O_4(OH)_3(H_2O)_6$, an electronic analogue to a Mo_3O_{13} cluster in $LiZn_2Mo_3O_8$, taken from ref.[1]. This shows a $S = 1/2$ arising in each molecule. This is consistent with (b), A band structure calculation on $LiZn_2Mo_3O_8$. Here, a Hubbard U of 2 eV was chosen for the calculations in (b) and (c), doped $LiZn_2Mo_3O_8$. As can be seen in (b), the band corresponding to the highest occupied molecular orbital in (a), once doped via the removal of Li in (c) shifts up in energy relative to the valence and conduction bands. While it is unphysical to apply a Hubbard U to a closed shell system in (c), the calculations were performed this way so that the undoped and doped band structures can be directly compared. These calculations suggest that upon doping, the energy level of the resulting hole increases in energy, thus favoring a form of Anderson Localization and an increase in the bandgap.

6 $LiZn_2Mo_3O_8$ Crystallographic and Local Structure

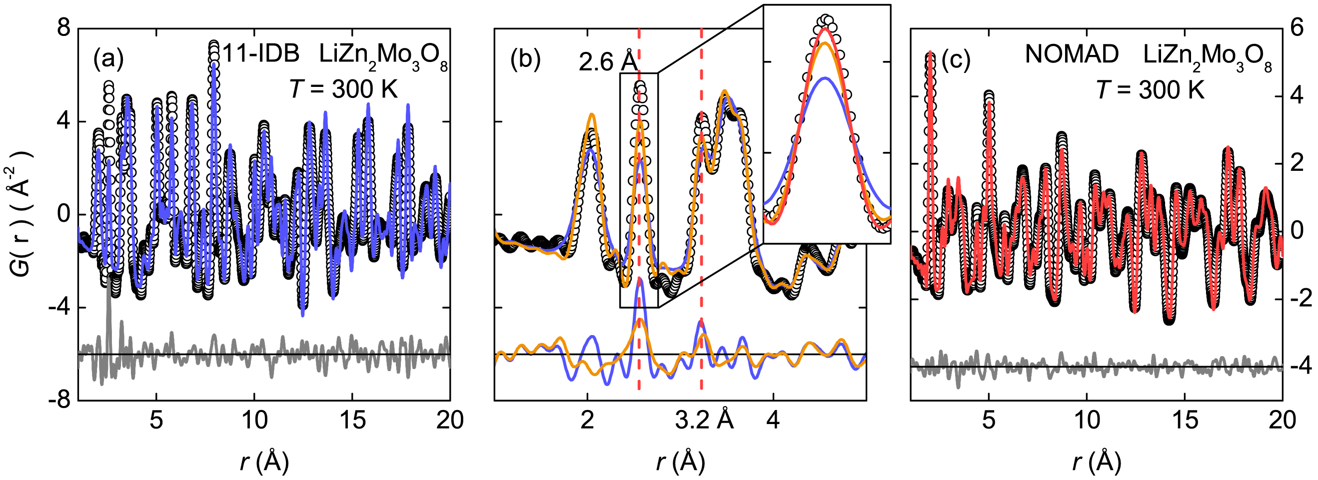

Figure 5 (a) Least squares fit to X-ray PDF data on $LiZn_2Mo_3O_8$ using the average $R\bar{3}m$ structure at T = 300 K. The fit is consistent with the calculated structure from the combined SXRD/NPD rietveld refinement, except for the large deviation from the data at low r, which is due to correlated motion effects. (b) The same refinement at $r \leq 5$ Å (blue line and difference curve) and a least squares fit to an overall $1/r$ correlated motion factor (orange lines). The two dashed red lines correspond to intra- (2.6 Å) and inter- (3.2 Å) Mo-Mo bond distances. Despite the refinement of the correlated motion factor in (b), the low r refinement is still poorly fit to the data. The inset shows the two fits (blue and orange lines) for the peak corresponding to the Mo-Mo intra-cluster peak at 2.6 Å. In addition, the red line is the original fit to the whole PDF [as in (a), the blue line] but with all parameters fixed and only the linear correlated motion parameter refined for the intra-cluster Mo-Mo peak. This indicates the correlated motion factor varies for different parts of the structure, namely Mo_3O_8 and the Li/Zn interlayers. This is expected, chemically, from the strong Mo-Mo bonding that is present. Note that such low r peak sharpening is inconsistent with a deviation of the local structure from trigonal symmetry, which would tend to broaden features in the PDF. (c) Least squares fit to neutron PDF data at T = 300 K. As opposed to the X-ray fit in (a), a single overall correlated motion factor results in a good fit to the data, suggesting that the correlated motion of the Mo_3O_8 is on a slower timescale than the interaction timescale of the neutrons.

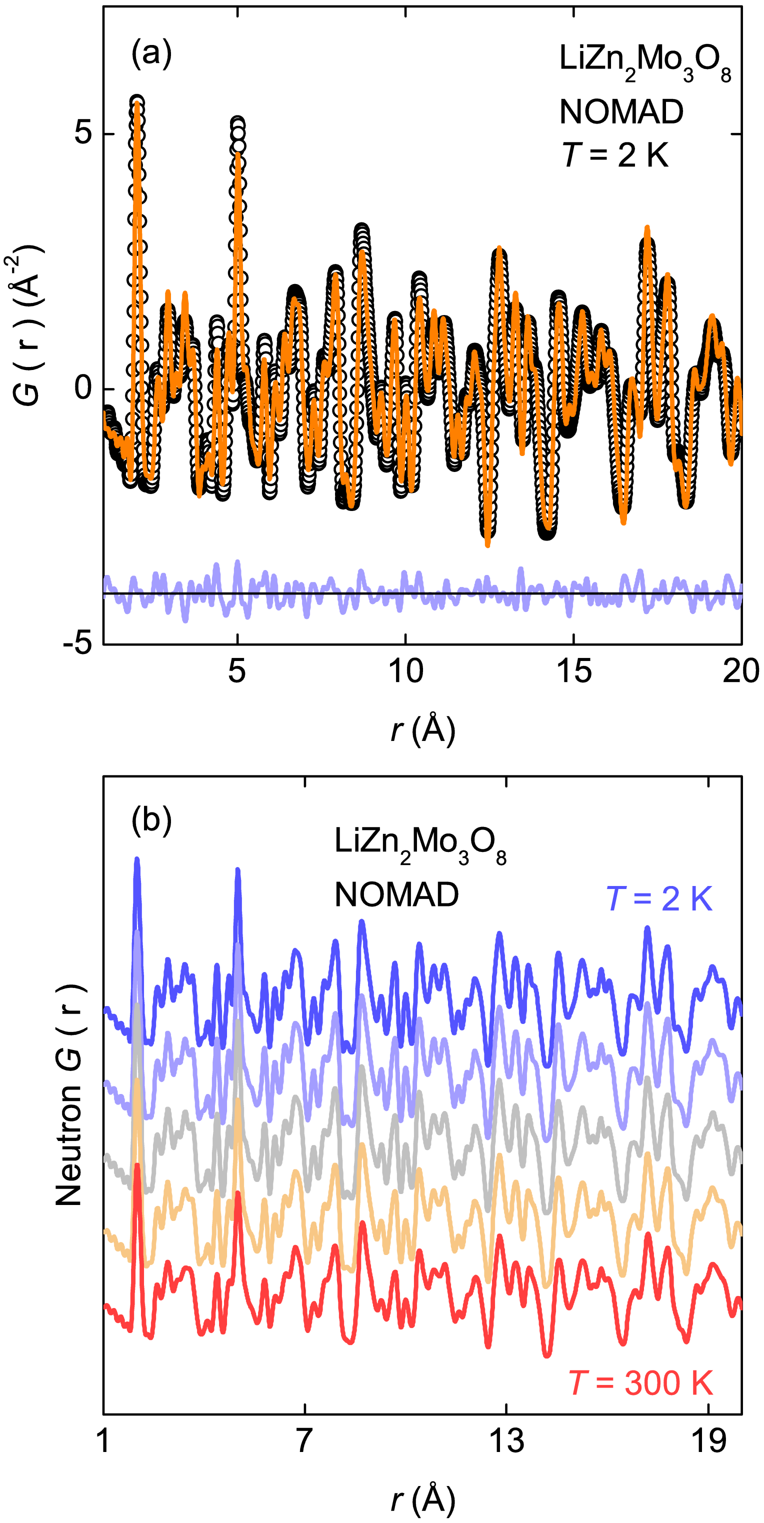

Figure 6 (a) Neutron PDF and corresponding least squares fit of undoped $LiZn_2Mo_3O_8$ at $T = 2\,K$, using refined average structure in $R\bar{3}m$. The average structure yields a good fit to the PDF over all ranges of r using an overall $1/r$ correlated motion factor as in Figure 5(c). (b) Neutron PDFs of $LiZn_2Mo_3O_8$ at various temperatures are surprisingly similar, with differences attributed only to the expected changes in thermal broadening, indicative of the lack of formation of any local structural distortions upon cooling down to $T = 2\,K$.

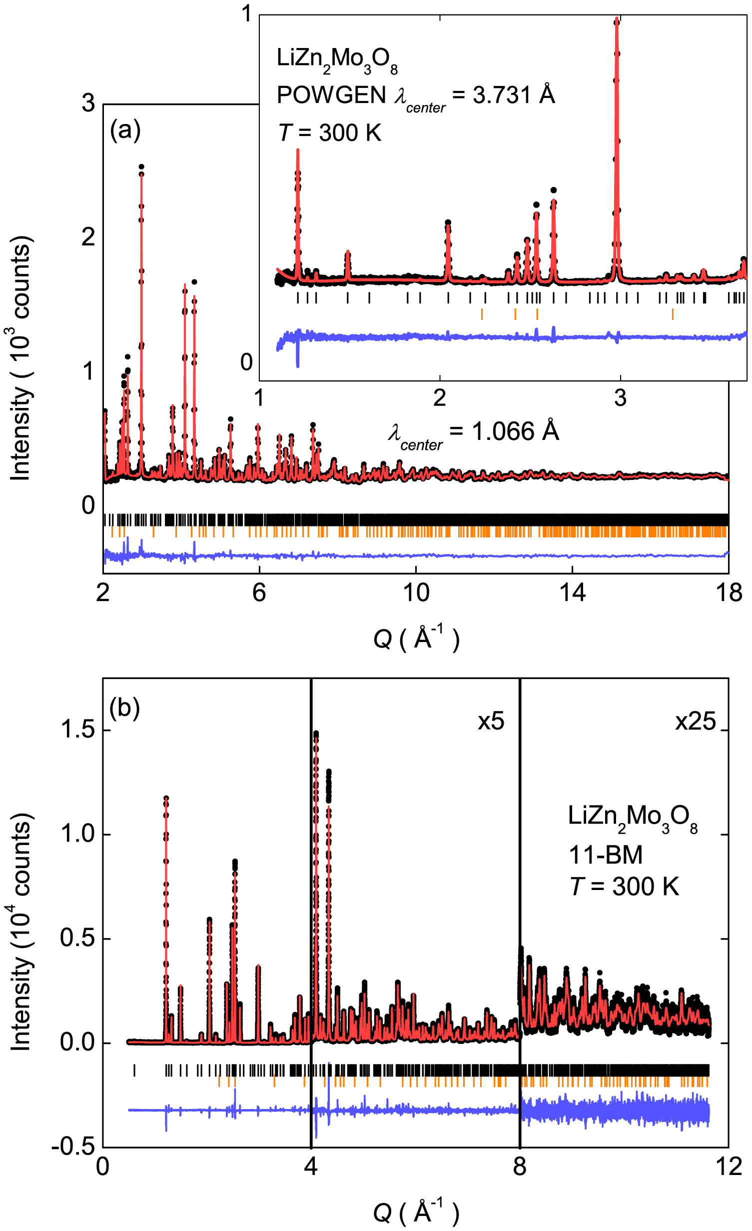

Figure 7 A joint Rietveld refinement to NPD (a) and SXRD (b) datasets on undoped $LiZn_2Mo_3O_8$. Black dots are observed data, red line is Rietveld fit, blue line is the difference, black tick lines correspond to $LiZn_2Mo_3O_8$ reflections in the $R\bar{3}m$ spacegroup, and orange lines are ZnO impurity reflections. Results are summarized in table 1 and table 2.

Table 1 Combined SXRD/Neutron refinement of $LiZn_2Mo_3O_8$ at T = 300 K

Chemical formula	$Li_{1.0(1)}Zn_{1.8(1)}Mo_3O_8$
Space group	$R\bar{3}m$
a(Å)	5.80163(3)
c(Å)	31.0738(2)
Z	6
Global weighted χ^2	6.870

Table 2 Atomic parameters of $Li_{1.0(1)}Zn_{1.8(1)}Mo_3O_8$ from joint SXRD/Neutron Rietveld refinement at T = 300 K

atom	x	y	z	Wyckoff position	Occupancy	U_{iso}
Mo-1	0.18504(8)	0.81496(8)	0.08393(4)	18*h*	1.0000	0.0016(2)
O-1	0.8445(2)	0.1555(2)	0.04850(6)	18*h*	1.0000	0.0017(3)
O-2	0.4920(2)	0.5080(2)	0.12438(7)	18*h*	1.0000	0.0047(4)
O-3	0	0	0.1185(1)	6*c*	1.0000	0.0054(7)
O-4	0	0	0.3715(1)	6*c*	1.0000	0.0053(6)
Zn-1	1/3	2/3	-0.64176(7)	6*c*	0.879(6)	0.0038(4)
Li-1	1/3	2/3	-0.64176(7)	6*c*	0.00(4)	0.0038(4)
Zn-2	0	0	0.1813(1)	6*c*	0.679(5)	0.0038(4)
Li-2	0	0	0.1813(1)	6*c*	0.22(4)	0.0048(4)
Zn-3	0	0	0	3*a*	0.265(7)	0.0038(4)
Li-3	0	0	0	3*a*	0.58(6)	0.0038(4)
Zn-4	0	0	0.5070(8)	6*c*	0.065(4)	0.0038(4)
Li-4	0	0	0.5070(8)	6*c*	0.43(3)	0.0038(4)
Li-5	2/3	1/3	0.08392(4)	6*c*	0.09(3)	0.0038(4)

7 Synchrotron X-ray analysis of $LiZn_{2-x}Mo_3O_8$ ($2x < 0.4$)

Table 3 Unit cell and fit statistics from $LiZn_{2-x}Mo_3O_8$ Rietveld refinements of 11-BM data at T = 6 K.

Sample (2x)	a(Å)	c(Å)	c/a	R_{wp}	LeBail R_{wp}	χ^2	LeBail χ^2
0.05	5.78148(2)	31.007(1)	5.36329(3)	11.96	10.09	5.48	3.96
0.10	5.78097(2)	30.997(1)	5.36198(3)	12.12	10.33	4.33	3.20
0.15	5.780(5)	30.98(3)	5.3605(7)	11.69	10.17	4.16	3.20
0.20	5.7794(2)	30.972(1)	5.35910(3)	11.68	10.14	3.92	3.03
0.25	5.7777(8)	30.954(4)	5.3575(1)	11.94	10.38	3.20	2.47
0.30	5.777(2)	30.947(1)	5.3562(2)	11.90	10.44	5.62	4.40
0.40	5.7763(1)	30.921(1)	5.35318(3)	11.90	10.35	4.75	3.65

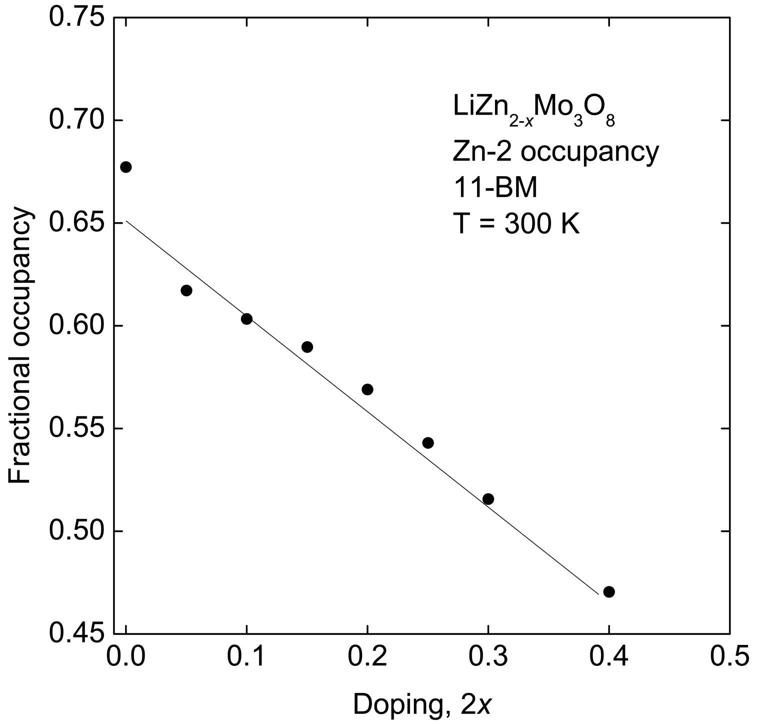

Figure 8 Occupation of the Zn-2 site obtained from Rietveld refinements of SXRD data. The line is a linear fit to the $x > 0$ data. The slope of this line, -0.45, shows that the bulk of the deintercalated zinc (90%) is removed from from the Zn-2 site.

References

[1] J. P. Sheckelton, J. R. Neilson, D. G. Soltan and T. M. McQueen, *Nature Materials*, 2012, **11**, 493496.

[2] A. Le Bail, *Powder Diffraction*, 2005, **20**, 316–326.

[3] J. Wang, B. H. Toby, P. L. Lee, L. Ribaud, S. M. Antao, C. Kurtz, M. Ramanathan, R. B. V. Dreele and M. A. Beno, *Review of Scientific Instruments*, 2008, **79**, 085105.

[4] H. M. Rietveld, *Journal of Applied Crystallography*, 1969, **2**, 6571.

[5] J. Rodrguez-Carvajal, *Physica B: Condensed Matter*, 1993, **192**, 55–69.

[6] X. Qiu, J. W. Thompson and S. J. L. Billinge, *Journal of Applied Crystallography*, 2004, **37**, 678.

[7] C. L. Farrow, P. Juhas, J. W. Liu, D. Bryndin, E. S. Boin, J. Bloch, T. Proffen and S. J. L. Billinge, *Journal of Physics: Condensed Matter*, 2007, **19**, 335219.

[8] K. Momma and F. Izumi, *Journal of Applied Crystallography*, 2008, **41**, 653–658.

[9] M. W. Schmidt, K. K. Baldridge, J. A. Boatz, S. T. Elbert, M. S. Gordon, J. H. Jensen, S. Koseki, N. Matsunaga, K. A. Nguyen, S. Su, T. L. Windus, M. Dupuis and J. A. Montgomery, *Journal of Computational Chemistry*, 1993, **14**, 1347–1363.

[10] B. M. Bode and M. S. Gordon, *Journal of Molecular Graphics and Modelling*, 1998, **16**, 133–138.